Spatiotemporal Mapping of Anisotropic Thermal Transport in GaN Thin Films via Ultrafast X-ray Diffraction: Supplementary Information

Thanh Nguyen,[1,12,*] Chuliang Fu,[1,12] Mouyang Cheng,[2,3] Buxuan Li,[4] Tyra E. Espedal,[5,6] Zhantao Chen,[7,8] Kuan Qiao,[4] Kumar Neeraj,[9] Abhijatmedhi Chotrattanapituk,[6] Denisse Cordova Carrizales,[1] Eunbi Rha,[1] Tongtong Liu,[5] Shivam N. Kajale,[10] Deblina Sarkar,[10] Donald A. Walko,[11] Haidan Wen,[9,11] Svetlana V. Boriskina,[4] Gang Chen,[4] Jeehwan Kim,[4,*] and Mingda Li[1,*]

[1] *Department of Nuclear Science and Engineering, Massachusetts Institute of Technology, Cambridge, MA 02139, USA*

[2] *Center for Computational Science and Engineering, Massachusetts Institute of Technology, Cambridge, MA 02139, USA*

[3] *Department of Materials Science and Engineering, Massachusetts Institute of Technology, Cambridge, MA 02139, USA*

[4] *Department of Mechanical Engineering, Massachusetts Institute of Technology, Cambridge, MA 02139, USA*

[5] *Department of Physics, Massachusetts Institute of Technology, Cambridge, MA 02139, USA*

[6] *Department of Electrical Engineering and Computer Science, Massachusetts Institute of Technology, Cambridge, MA 02139, USA*

[7] *Linac Coherent Light Source, SLAC National Accelerator Laboratory, Menlo Park, CA 94025, USA*

[8] *Stanford Institute for Materials and Energy Sciences, Stanford University, Stanford, CA 94025, USA*

[9] *Materials Science Division, Argonne National Laboratory, Lemont, IL 60439, USA*

[10] *MIT Media Lab, Massachusetts Institute of Technology, Cambridge, MA 02139, USA*

[11] *Advanced Photon Source, Argonne National Laboratory, Lemont, IL 60439, USA*

[12] *These authors contributed equally to this work.*

(Dated: July 1, 2025)

* Corresponding authors. ngutt@mit.edu, jeehwan@mit.edu, mingda@mit.edu

This supplementary file contains the following elements:

Supplementary Text with Sections S1 to S13

Figs. S1 to S11

Table S1

Contents

S1. Additional images of the GaN thin film on silicon

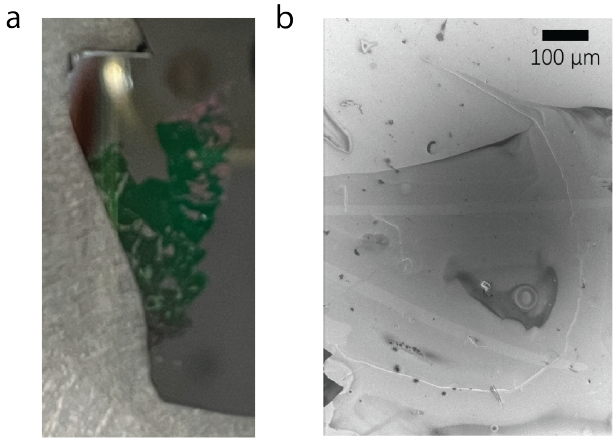

Figure S1. **a.** Camera image of the GaN thin film (in green) after being transferred onto the piece of silicon substrate using heat and pressure. **b.** Scanning electron microscope image of the GaN thin film visualizing wrinkles and other local imperfections. The scale bar indicates the length of 100 μm.

S2. Single-gated versus double-gated mode acquisition

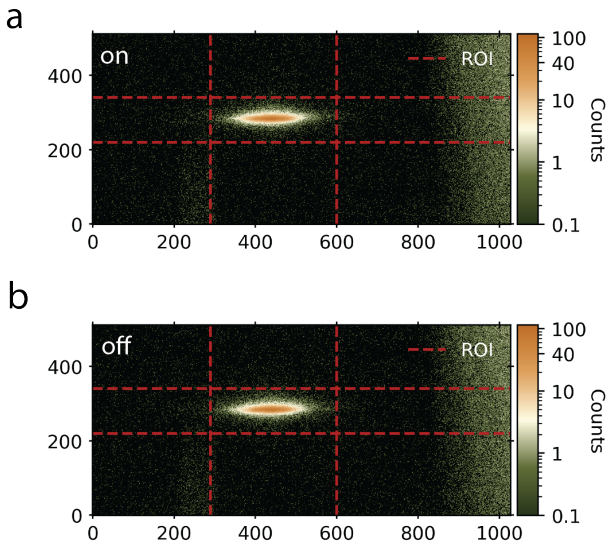

Figure S2. Two-dimensional pixel array detector image on the Eiger taken of the (002) Bragg peak **a.** after and **b.** before the arrival of the optical pump laser (at $\Delta t = 1$ ns). Here, the peak shifts upon photoexcitation by ∼1 pixel upwards – corresponding to a 2θ change of arctan(75 μm/700 mm) = 6 mdeg.

In our time series measurements at a constant fluence and pump-probe distance Δx, in double-

gated mode, we collect two two-dimensional detector array images at each pump-probe time delay Δt: one before and one after the optical pump (Fig. S2). In single-gated mode, with higher throughput, we only take a detector snapshot after the optical pump. For the majority of the experiment, we opt for the double-gated mode. The double-gated mode, while not drastically very different from the information of single-gated mode as shown in Fig. S3, does remove a gradual linear time-dependence of the static Bragg peak in the absence of photoexcitation. The slow linear-in-time off signal tends to skew the time constant of the decaying relaxation to shorter time constants so we take care to correct this effect. Furthermore, double-gated mode removes artifacts that arise from the occasional refilling of the synchrotron with electron bunches and observed in the data as sharp spikes in intensity. More data points were taken at small Δt to accurately capture the short time photoinduced dynamics.

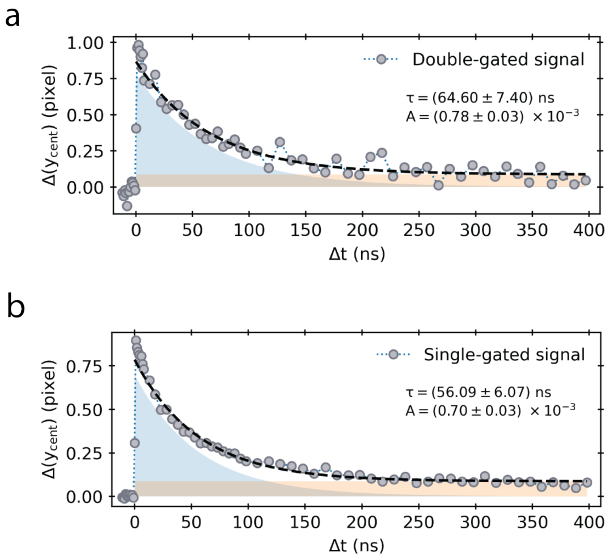

Figure S3. **a.** Signal from the double-gate mode where the y-centroid of the on-pulse image is subtracted from that of the off-pulse image for improved signal-to-noise and removal of gradual time effects. The on and off images correspond to those shown in Figs. 1 in the main text and S2. A fit to an exponential decay on top of a constant (blue dashed line) is shown along with the individual function contributions in shaded regions. Error values are obtained from propagating counting statistics-related error and from the fit. **b.** Similar as in **a.**, but with the single-gated mode. We note the smaller time constant compared to the double-gated mode.

S3. Intensity and width change of the signal from the pump

In the main text, we show the signal derived from the peak shift upon photoexcitation. Here, in this supplementary note, we show how the integrated intensity and the full width at half maximum (FWHM) of the Bragg peak on the two-dimensional array detector change with pump-probe time decay Δt dependence. From the two-dimensional array obtained from the detector, we fit a two-dimensional Gaussian profile to the peak of the image to extract the integrated peak intensity and the peak FWHM (averaging the FWHM along the two directions and propagating the error bar). In the following plots, we plot the change in 2θ angle that was converted from the y-centroid shift by noting the individual pixel size and the distance between the detector and the sample (as $\arctan(75(\Delta\text{pixel})\times 10^{-6}/700\times 10^{-3})$ where Δpixel is the shift in pixels). As shown below, the integrated intensity (normalized to the maximum intensity) varies insignificantly with Δt on top of the gradual drift described previously, only changing by a few percent within error bars (Fig. S4).

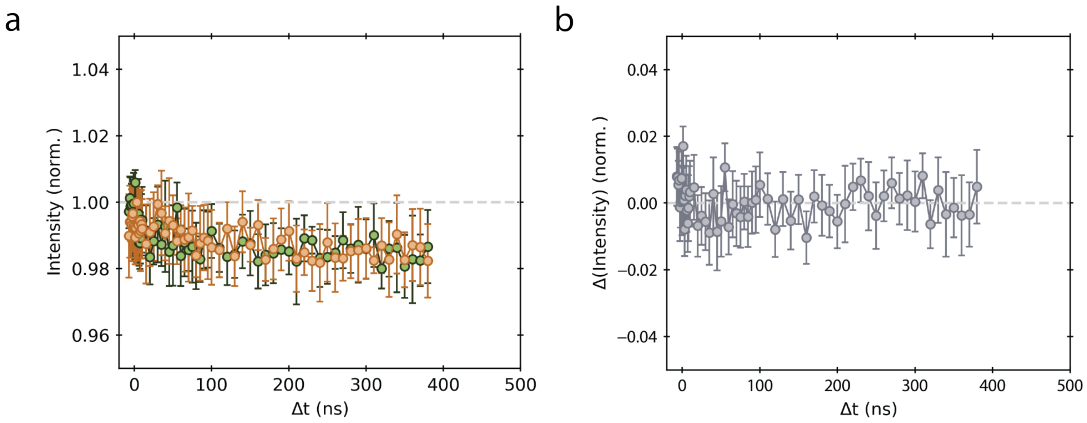

Figure S4. **a.** Integrated intensity normalized to maximum peak value as a function of pump-probe time delay Δt when the pulse is on (green) and off (orange). **b.** Difference plot of **a.**. Error bars represent one standard deviation and originate from Poisson counting statistics.

By contrast, the FWHM of the Bragg peak does manifest a noticeable change as a function of pump-probe time delay Δt. We show, in Fig. S5, plots of the FWHM and the difference between instances when the optical pump is on and off. The signal decays at a much shorter time constant (< 20 ns) in comparison to the 2θ shift signal. We also note that this signal using the FWHM is only apparent at large enough fluence levels of the optical pump (including the fluence level we ran at for most of the experiment) and does not appear when the laser power is small. These observations suggests a generation of electronic strain or of coherent ballistic phonons at this shorter time scale compared to the longer diffusive thermal processes. The FWHM value and the change in FWHM

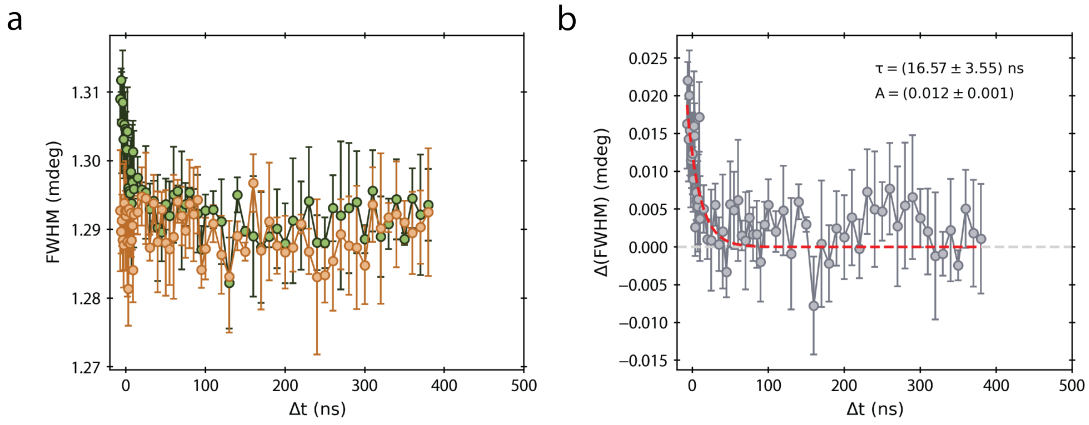

Figure S5. **a.** Full width at half maximum (FWHM) value as a function of pump-probe time delay Δt when the pulse is on (green) and off (orange). **b.** Difference plot of **a.**. Error bars represent one standard deviation and originate from Poisson counting statistics. A exponential fit (red dashed line) is added with fitted values and their errors displayed.

are small ($\sim$1 mdeg and $\sim$0.02 mdeg, respectively) compared to the 2θ shift (reaching 6-10 mdeg).

S4. Fitting model of time series measurements

As mentioned in the previous supplementary notes, it would seem that the pump-probe time delay dependence of the 2θ shift would reveal two concurrent processes with distinct time scales. A hint of this hypothesis comes from the FWHM difference signal with a sub-20 ns time constant. Here, we demonstrate fits to the time series measurements using two models: 1) a double exponential with two different time constants and 2) an exponential added onto a constant value. As shown in Fig. S6, the model that includes the second exponential function improves the fit significantly (as shown by the χ^2 value), especially at the low time scales seen in the semi-logarithmic plot. We interpret the signal as having a small timescale component from electronic or ballistic phonon-induced strain and a long timescale component from diffusive relaxation of the lattice. We note that the contribution to the signal from the exponential with the smaller time constant becomes larger as the fluence level increases, i.e. the 2θ at early times becomes sharper at higher fluences. This indicates that it is related to a process that depends on the fluence of the optical laser – which would be consistent with the picture of electronic strain due to more generated charge carriers. The exponential with long time constant, which we associate with the diffusive process, is characterized by $\tau > 60$ ns. For our thermal modeling of the experiment, we use this two-component analysis to support our simplified initial temperature profile by extracting out the early-time portion of the experimental data.

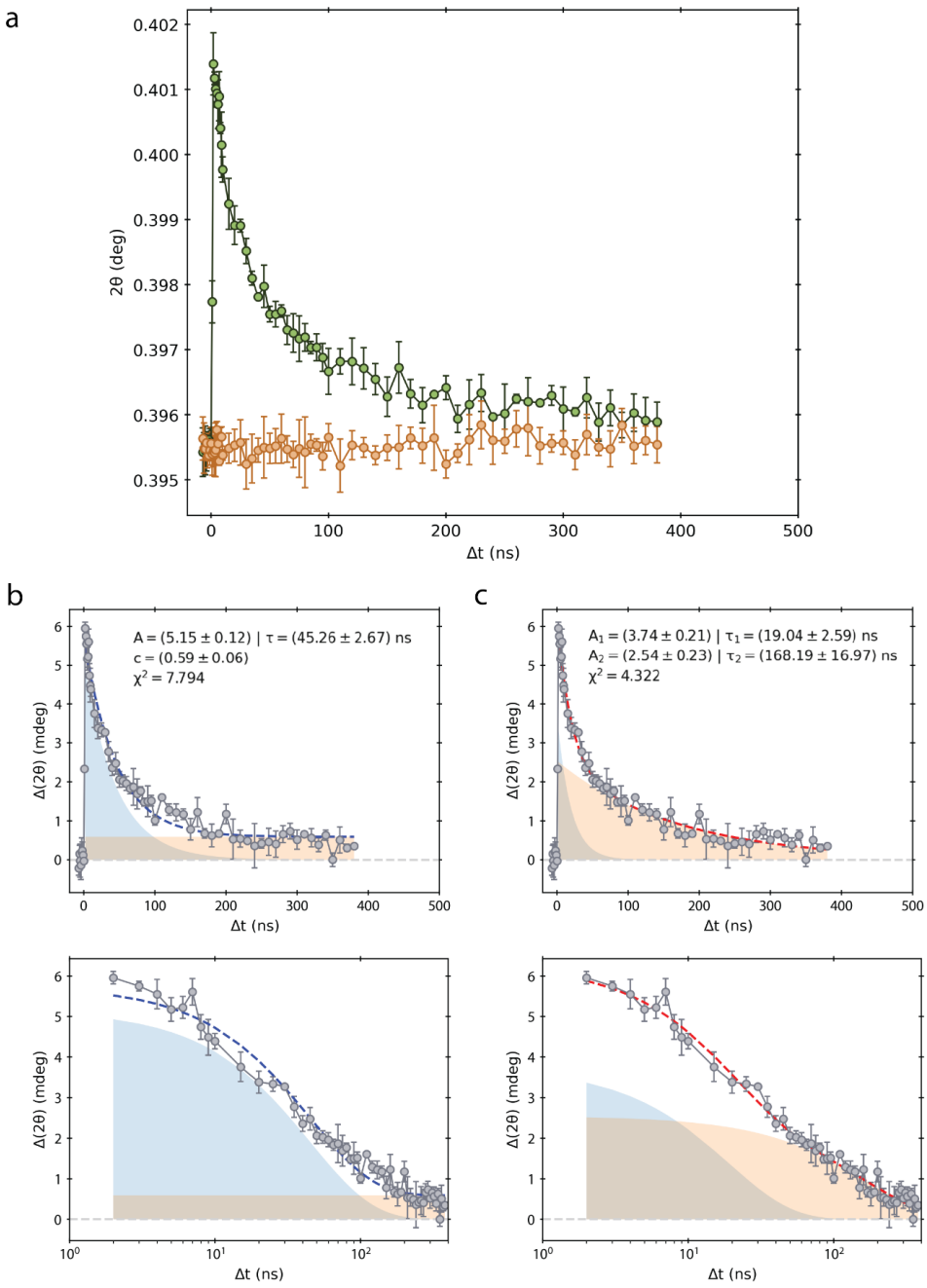

Figure S6. **a.** Plot of the 2θ value of the Bragg peak as a function of pump-probe time delay Δt with the pump on (green) and off (orange). The value of the y-axis corresponds to the distance away from the center of the detector and not the actual 2θ value. **b.** Linear (top) and semi-logarithmic (bottom) difference plot with a fit involving an exponential added to a constant value. **c.** Linear (top) and semi-logarithmic (bottom) difference plot with a fit involving two exponential functions with a small and large time constant, respectively. In all plots, error bars represent one standard deviation that is propagated from Poisson counting statistics. Fit parameters (and their errors) and chi-square values are displayed for each corresponding fit. Contributions to the signal from each function component of the model are shown in shaded regions.

S5. Fluence dependence of the optical pump laser

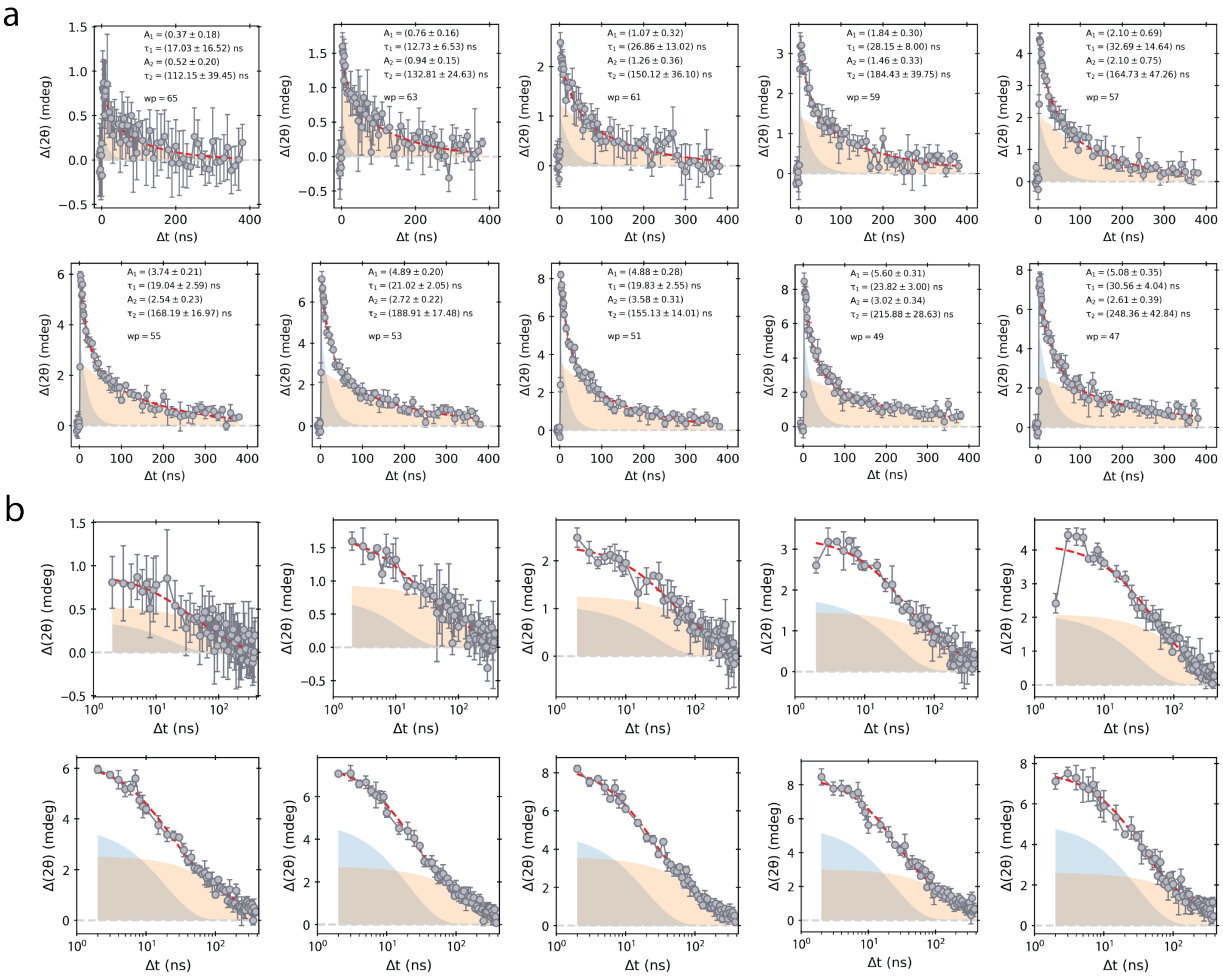

Figure S7. **a.** Plots of the 2θ angular shift as a function of pump-probe time delay Δt at different waveplate angles (and thereby, different fluence levels) from 65° to 47° and at spatial coincidence between the pump and probe ($\Delta x = 0$). **b.** Corresponding plots as in **a.**, but with the Δt axis on a logarithmic scale. Fits are based on the double-exponential model described in previous sections. Fit parameters and their error bars are displayed. Error bars represent one standard deviation and originate from Poisson counting statistics.

Fig. S7 displays the fluence dependence of the optical pump on the time series measurements of the 2θ angular shift. A few trends can be observed. As the fluence increases (waveplate angle decreases), the maximal 2θ angular shift immediately near $\Delta t = 0$ increases monotonically up to a certain value of 53° or 51° after which the value saturates. This is due to sample degradation at high fluence which was also observe visually by eye on the sample as lines indicating sample burn. Furthermore, as the fluence increases even beyond the saturation point, the sharpness of the drop in the early time signal increases which can be observed as a larger contribution of the low-time-scale

exponential function and the longer decay time for the second exponential. These observations hint at a fluence-dependent mechanisms for the early time scales such as an electronic strain. As mentioned in the main text, we chose to run the majority of the experiment at a waveplate angle of 55° which sits below the value at which the maximum 2θ angular shift saturates.

S6. Angular shift at large pump-probe distances and laser intensity profile

In Fig. S8, we plot the 2θ angular shift where the distance between the pump laser and the x-ray probe is 13 μm. Here, we sum over thirteen measurements of the time series to improve the statistics. The fitting error remains relatively substantial at these large pump-probe distances. The maximum 2θ angular shift is 0.46 mdeg which corresponds to a lattice constant change of 6.5 fm or equivalently, a strain value of 1.25×10^{-5}.

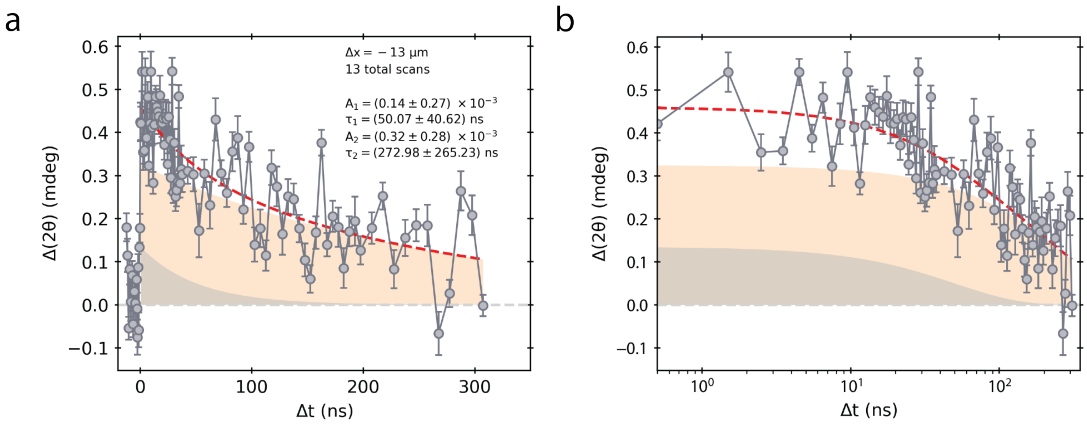

Figure S8. **a.** Plot of the 2θ angular shift versus pump-probe delay time at a spatial distance of $\Delta x = 13$ μm between the pump and probe from the sum of thirteen time series measurements. **b.** Corresponding plot with the Δt-axis in logarithmic scale. The red dashed line indicates a fit to a double-exponential function. Error bars indicate one standard deviation from Poisson statistics.

To ensure that the angular shift measured in our experiment is not purely due to the intensity profile of the optical laser, we perform a knife edge scan to measure the profile of the beam. We scan a knife edge across the face of the beam while measuring the power. The power drops as the knife edge blocks progressively more of the beam, thereby enabling us to relate the measured power as a function of the knife edge position with a beam radius. As shown on the left of Fig. S9, we plot the laser power versus the y position of the piezostage controlling the laser position which displays a

characteristic complementary error function form (as expected for a Gaussian-shaped beam) with

$$\frac{P(z)}{P_{\max}} = \frac{1}{2}\mathrm{erfc}\left(\frac{z}{\sigma}\right) \tag{S1}$$

where z is the position, σ is the beam width, and erfc is the complementary error function ($1 - \mathrm{erf}$, with erf being the normal error function). When a fit is of the form above is applied to the data, a beam width of (13.3 ± 0.8) μm is extracted. We showcase the reconstructed beam intensity profile on the right of Fig. S9 from the knife edge scan and plot the maximum 2θ shift immediately after the optical pump for different Δx.

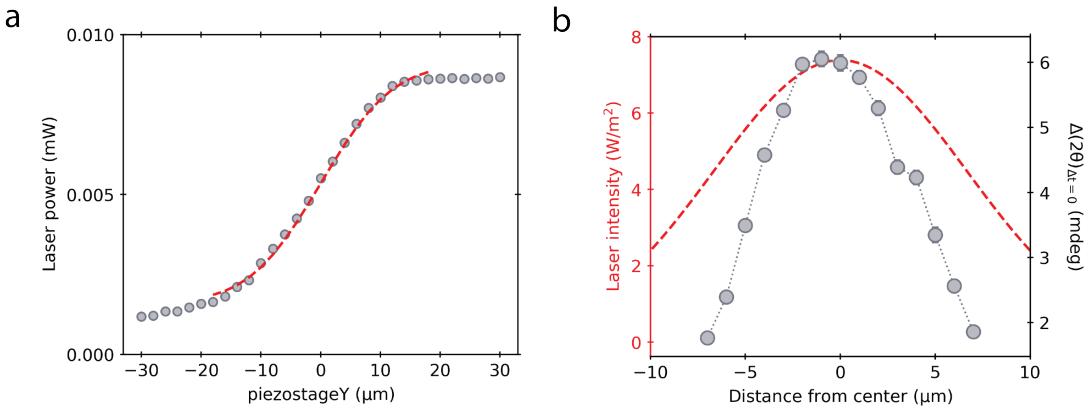

Figure S9. **a.** Knife edge scan of the beam profile for the optical pump laser. A fit is shown as a red dashed line to extract the beam width. **b.** Re-constructed beam profile of the optical pump from the knife edge scan as a red dashed line (left axis) and maximum angular shift as a function of pump-probe distance immediately after the optical pump ($\Delta t = 0$) in grey data points (right axis). The beam profile is considerably larger than that of the angular shift.

While there is a slight correlation between the spatial-dependence of the angular shift with the beam intensity profile, the beam profile of the optical pump does not match that of the angular shift which has a smaller characteristic width – thereby suggesting that other factors may explain the discrepancy. We argue that the angular shift observed in the experiment does not originate from the beam profile, but rather, most prominently, from the heat dissipation in the thin film due to this discrepancy in profile shape. Notably, it should be emphasized that in the cases where a wrinkle is involved, one can observe a clear distinction in angular shift signal between equivalent distances ($\Delta x \pm 3$ μm) depending on whether the wrinkle is there or not, which would not be explainable if the effect were purely from the beam profile.

S7. Scans of the optical pump laser positions along the orthogonal direction

To verify the isotropic nature of the laser-induced heat at the center of our region of interest on the thin film, we also perform time series measurements along different positions in the orthogonal direction (forming a cross shape with the measurements in the main text). Along the $\Delta x = 0$ line, we perform measurements at 1.5 μm steps in the vertical direction at different Δy, which are shown in Fig. S10. The spatial step size is larger in the Δy direction compared to the Δx direction because the objective used in focusing the pump laser has a 3:2 scale between the optical pump distance and the actual distance of the laser spot on the thin film. We observe similar behavior compared to the horizontal positional scans which suggest that the heat dissipated from the laser spot is isotropic in the lateral directions.

S8. Conversion of angular shift to local temperature

To convert the angular shift of the (002) Bragg peak of GaN into a local temperature T_{loc} which will be used in our calculations involving the heat conduction equation, we use the following procedure. The initial temperature profile is directly extracted from the experiment measurements immediately after $\Delta t = 0$. To obtain the temperature profile, we first convert $\Delta(2\theta)$ into a lattice constant change Δc using Bragg's law ($\lambda = 2d\sin(\theta)$). Here, $\lambda = 1.13$ Å (11 keV x-ray probe) and d can be obtained, for a hexagonal structure like the case of GaN, with $1/d^2 = (3/4)(h^2 + hk + k^2)/a^2 + l^2/c^2$ where $(hkl) = (002)$, $a = 3.190$ Å, $c = 5.189$ Å, and $2\theta = 23.8°$ for our measurement. Afterwards, we can obtain the local temperature value using the linear thermal expansion coefficient α and relating the strain ($\Delta c/c$ or $\Delta(\theta)/\theta$) to the temperature with the formula

$$\cot(\theta)\Delta\theta = -\alpha\Delta T. \tag{S2}$$

We set the boundary condition of the two ends of the thin film to be set at the fixed temperature of 300 K, which is the temperature of the experiment.

It is worth to mention that the out-of-plane expansion can be enhanced by a factor involving the Poisson ratio while the in-plane expansion may be forced to zero as it is epitaxially clamped to the substrate. As a result, the relation between strain and temperature should be $\Delta c/c = (1+\nu)/(1-\nu)\alpha\Delta T$ where $\nu = 0.18$ is the Poisson ratio of GaN. However, after the numerical simulation and the fitting, we notice this correction of this conversion does not affect the fitted thermal parameters. The fitted in-plane thermal conductivity ranges to $k_{\parallel}$ =(93.8 ± 22.0) W/m·K for the corrected conversion compared to the original fitted (92.8 ± 22.0) W/m·K. The fitted localized wrinkle thermal conductivity

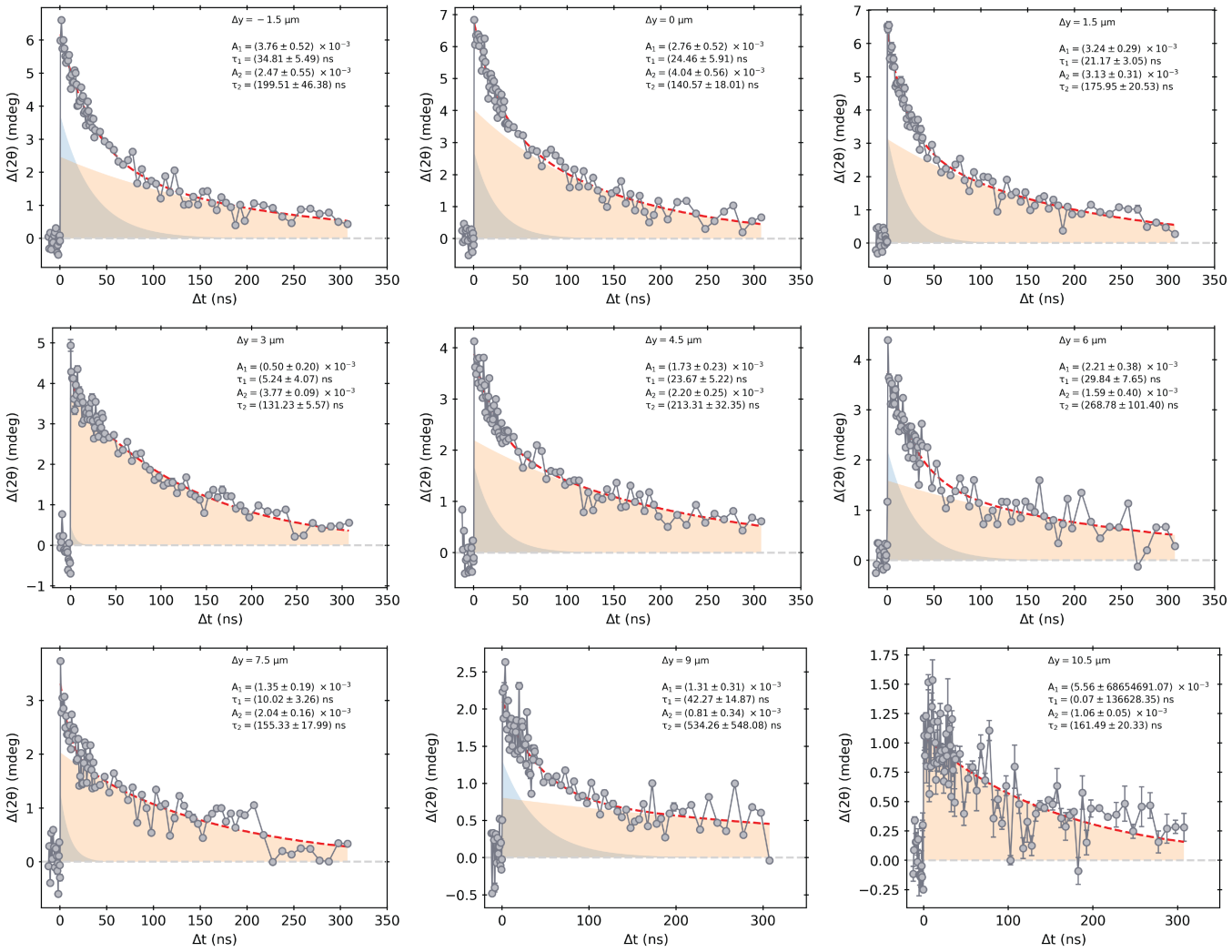

Figure S10. Plots of the 2θ angular shift at different values of pump-probe distance in the vertical direction (Δy) along the $\Delta x = 0$ line on the thin film as a function of pump-probe time delay. Values of $\Delta y = -1.5$ μm to $\Delta y = 10.5$ μm are shown in steps of 1.5 μm. Note here Δy is not the vector along y-axis, but the relative displacement between the pump and the probe perpendicular to the relative displacement Δx between pump and probe. Fits are using a double-exponential function. Error bars represent one standard deviation from Poisson statistics.

for the corrected conversion $k_w = (20.7 \pm 0.4)$ W/m·K compared to $k_w = (21.2 \pm 1.2)$ W/m·K and the GaN-Si TBC value near the wrinkle defect of $G_w = (2.10 \pm 0.05) \times 10^7$ W/m^2·K compared to $G_w = (2.12 \pm 0.05) \times 10^7$ W/m^2·K. This small improvement may be due to the small Poisson ratio of GaN and the robustness of the whole numerical workflow. The other fitting information for the corrected conversion of the data to the temperature are also attached in the other Supplementary sections.

S9. Theoretical model

A. Three-dimensional heat transport

In this subsection, we analyze the transport mechanism that occurs within the materials of the experiment described in this work. The size of the thin film system is on the scale of microns with a thickness of 500 nm, and the phonon mean free path is at most around 100 nm. The latter is smaller in both the in-plane and cross-plane directions. The heat diffusion characteristic time $t_c \approx l^2/D$ is around several nanoseconds, matching the time scale in the experiments, where D is the thermal diffusivity. This can be estimated as $D = k/\rho C$ where $k > 0$ is the thermal conductivity, ρ is the mass density, and C is the specific heat capacity.

As a result, the thermal transport mechanism should be diffusion-dominated and can be described by Fourier's law and the heat conduction equation [1]. The general heat conduction equation is

$$C\rho\frac{\partial T(\mathbf{r},t)}{\partial t} = \nabla\cdot(\overleftrightarrow{\mathbf{k}}\nabla T(\mathbf{r},t)), \tag{S3}$$

where $T(\mathbf{r},t)$ is the local effective temperature with dependencies on position $\mathbf{r}$ and time t, C is the heat capacity, and ρ is the mass density. This equation governs the transport behavior for $\mathbf{r}\in\Omega$ where Ω is the area within the material. Here, $\overleftrightarrow{\mathbf{k}}$ is typically a thermal conductivity tensor, but we take a simplified case by assuming that the non-diagonal part vanishes. In this case, only the diagonal elements $k_{xx} = k_{yy} = k_\parallel$, and $k_{zz} = k_\perp$ are nonzero in which $\overleftrightarrow{\mathbf{k}}$ has spatial dependence.

$\mathbf{r}\in\partial\Omega$ represents the boundary or, in our case, the junction or contact between different materials. For the experiment described here, $\partial\Omega$ is the contact area between the GaN thin film and the Si substrate. We discuss how to solve for this boundary in the following subsection using a thermal boundary conductance (TBC) simulation.

B. Boundary condition: Simulate TBC using the heat conduction equation

In general, we should consider the TBC along the cross-plane direction at the boundaries between different materials. For our material system, we only need to consider the main interface between GaN and Si, which otherwise can be further generalized in principle into a system with multiple interfaces. TBC is defined as the thermal flux per unit area per temperature difference. This can be expressed through the boundary condition

$$\begin{aligned} -k_{zz,\mathrm{GaN}}\frac{\partial T_{\mathrm{GaN,b}}}{\partial z^+} &= G_{\mathrm{GaN,Si}}\left(T_{\mathrm{Si,b}} - T_{\mathrm{GaN,b}}\right), \\ -k_{zz,\mathrm{Si}}\frac{\partial T_{\mathrm{Si,b}}}{\partial z^-} &= G_{\mathrm{GaN,Si}}\left(T_{\mathrm{GaN,b}} - T_{\mathrm{Si,b}}\right). \end{aligned} \tag{S4}$$

$G_{\mathrm{GaN,Si}}$ is the TBC of the interface between Si and GaN. A subscript b represents the spatial location on the contacting boundary layer between the GaN thin film and the Si substrate. It indicates the position at the bottom of GaN and the top of the Si substrate Si. $T_{\mathrm{Si,b}}$ and $T_{\mathrm{GaN,b}}$ are the temperature profiles at the contacting boundary layer for Si and GaN, respectively. As a result, this boundary condition provides a normal vector of the temperature gradient along the out-of-plane direction.

C. Initial condition: Simplified initial profile

In these calculations, we set the mass density of GaN as $\rho = 6.08$ g/cm^3 and the heat capacity as 35.4 J/(mol·K). The characteristic thermal redistribution time along the cross-plane direction for the thin GaN film is estimated to be approximately 8 ns if we assume that the cross-plane thermal conductivity is 80 W/(m·K) which is close to the upper bound measured from our TDTR experiments. This implies that the film requires this period to reach thermal equilibrium along this direction.

To simplify the problem, we neglect the first couple of nanoseconds which allows the temperature profile within the thin film to fully redistribute. Both the FWHM measurement and other experimental observations suggest the presence of electronic strain effects which may potentially arise from complex electron-photon interactions that occur on shorter timescales than thermal diffusion. To ensure a more accurate comparison between the simulation and the experimental data, the introduction of a delayed initial time is reasonable to account for these strain effects. This approach minimizes the influence of the latter provided that the delay is not excessive as cross-plane heart transport between the thin film and the substrate remains minimal, while ensuring that the initial temperature profile remains accurately represented. Consequently, we can model the cross-plane transport as a two-timescale problem where the thermal redistribution within the thin film occurs rapidly on a small timescale whereas the heat conduction along the substrate and the heat transfer between the thin film and the substrate are comparatively slower on longer timescales. If we neglect the rapid initial phase and focus only on the slower dynamics, we can simplify the problem by adopting a coarser spatial mesh (on the order of microns like our experiment) and redefining the initial time.

In this case, the substrate can be reasonably assumed to remain at room temperature as the early-stage heat transfer from the thin film to the substrate is minimal and the TBC is relatively low. One must take note that this approach may lead to a slight underestimation of thermal parameters as it involves a necessary trade-off in accuracy for the sake of computational efficiency.

S10. Theoretical model for wrinkle-affected thermal transport

We describe how we modify the thermal model to include the effect caused by the presence of a wrinkle on the thin film. To simplify the discussion without loss of generality, we consider the situation in one dimension along the in-plane direction (such as along the x direction) and then generalize to the three-dimensional case later on. We consider that the presence of the wrinkle would affect the thermal conductivity $k_{\parallel}$ locally, leading to spatial inhomogeneity of the thermal conductivity. As a result, we rewrite spatially dependent $k_{\parallel} = k_{\parallel,\mathrm{hom}} + Q(x, x_w, \epsilon)\Delta k_w$ where x_w is the position of the wrinkle, $k_{\parallel,\mathrm{hom}}$ is the homogeneous thermal conductivity, Δk_w is the wrinkle-induced change of the thermal conductivity, and $Q(x, x_w, \epsilon) = \exp\left(-\frac{(x-x_w)^2}{2\epsilon^2}\right)$ is the Gaussian kernel function with positional parameter x_w and width parameter ϵ. The latter is a small parameter used to control the global and local coupling. When $x = x_w$, we define $k_w = k_{\parallel,\mathrm{hom}} + \Delta k_w$. This treatment can be considered as a multiscale modeling to resolve singularities as shown in Ref. [2]. After inserting the wrinkle-induced term back into the original equation, we obtain

$$\begin{aligned} C\rho\frac{\partial T}{\partial t} &= k_{\parallel}\frac{\partial^2 T}{\partial x^2} + \frac{\partial k_{\parallel}}{\partial x}\frac{\partial T}{\partial x} \\ &= k_{\parallel,\mathrm{hom}}\frac{\partial^2 T}{\partial x^2} + Q(x_w,\epsilon)\left(\Delta k_w\frac{\partial^2 T}{\partial x^2} - \Delta k_w\frac{2(x-x_w)}{2\epsilon^2}\frac{\partial T}{\partial x}\right) \\ &\approx k_{\parallel,\mathrm{hom}}\frac{\partial^2 T}{\partial x^2} + \delta_{x,x_w}W, \end{aligned} \tag{S5}$$

where $W = \Delta k_w(\partial^2 T/\partial x^2) - \Delta k_w((2(x-x_w))/(2\epsilon^2))(\partial T/\partial x)$ can be considered as a source term, which contains dependencies on $\Delta k_w(\partial T/\partial x)$ and $\partial^2 T/\partial x^2$. If we assume the parameter ϵ is small, then the Gaussian kernel function can be approximated as δ_{x,x_w}. In the numerical calculation presented later on, as space is discretized, we can linearly approximate the kernel with a trapezoid with $Q \approx 1 - |x - x_w|/(2\epsilon)$ if $|x - x_w| \leq 1$ and $Q = 0$ otherwise. We can attribute and model the effect of the wrinkle as a temperature profile-dependent point-like source or sink. The temperature profile-dependent heat source/sink induced by the presence of the wrinkle may lead to non-reciprocal thermal transport. The latter was inferred from asymmetrical measurements in our experiment and confirmed through our numerical calculations. By generalizing to the three-dimensional case, we have

$$C\rho\frac{\partial T}{\partial t} = k_{xx}\frac{\partial^2 T}{\partial x^2} + \frac{\partial k_{xx}}{\partial x}\frac{\partial T}{\partial x} + k_{yy}\frac{\partial^2 T}{\partial y^2} + k_{zz}\frac{\partial^2 T}{\partial z^2} \approx \nabla\cdot(\overleftrightarrow{\mathbf{k}}_{\mathrm{hom}}\nabla T) + \delta_{x,x_w}W \tag{S6}$$

where we have assumed the defect-cased heterogeneity only arises along the x-axis and that the defect acts as a heat source or sink in the three-dimensional case, here $\overleftrightarrow{\mathbf{k}}_{\mathrm{hom}}$ is the homogeneous thermal conductivity tensor.

We briefly explain with a microscopic picture. Without loss of generality, we discuss the situation with a one-dimensional picture (along the x axis) with general thermal conductivity k, homogeneous

thermal conductivity k_{hom}, the change of thermal conductivity caused by wrinkle Δk_w, the thermal conductivity k_w at the wrinkle, while a similar one can also apply in three dimensions. The thermal conductivity can be characterized through the Callaway model with the isotropic and single-mode approximation as

$$k = \frac{1}{3}\int_0^{\omega_{\max}} C_s(\omega)\tau(\omega)v_g^2(\omega)\ d\omega \tag{S7}$$

where C_s is the spectral heat capacity, τ is the relaxation time, and v_g is the phonon group velocity. The wrinkle emerges as a spatial-dependent contribution for this term. We consider that the region close to the wrinkle can be described with a wrinkle-induced phonon scattering rate (τ_{pw}^{-1}), phonon-phonon scattering rate (τ_{pp}^{-1}), and phonon-impurity scattering rate (τ_{pd}^{-1}) such that $\tau_w^{-1} = \tau_{pw}^{-1} + \tau_{pp}^{-1} + \tau_{pd}^{-1}$. In the non-singularity region, we only have the phonon-phonon scattering rate and the phonon-impurity scattering rate such that the corresponding homogeneous relaxation rate is $\tau_{\text{hom}}^{-1} = \tau_{pp}^{-1} + \tau_{pd}^{-1}$.

The corresponding expressions for the thermal conductivity are given by

$$\begin{aligned} k_{\text{hom}} &= \frac{1}{3}\int_0^{w_{\max}} C_s(\omega)\tau_{\text{hom}}(\omega)v_g^2(\omega)\ d\omega \\ \Delta k_w &= \frac{1}{3}\int_0^{\omega_{\max}} (\tau_w(\omega) - \tau_{\text{hom}}(\omega))v_g^2(\omega)\ d\omega \\ k_w &= \frac{1}{3}\int_0^{w_{\max}} C_s(\omega)\tau_w(\omega)v_g^2(\omega)\ d\omega \end{aligned} \tag{S8}$$

where k_w designates the thermal conductivity at the exact position of the wrinkle. The total thermal conductivity can be rewritten as

$$k = k_{\text{hom}} + Q(x_w,\epsilon)\Delta k_w = \frac{1}{3}\int_0^{\omega_{\max}} C_s(\omega)(\tau_{\text{hom}} + Q(x_w,\epsilon)(\tau_w(\omega) - \tau_{\text{hom}}))v_g^2(\omega)\ d\omega. \tag{S9}$$

The defect region can be considered as a perturbation of the original thermal conductivity, coupling with both the singularity and the homogeneous region. The spatial coupling can be effectively achieved by adding the function $Q(x_w,\epsilon)$ as the strength coefficient. We can assume that the wrinkle-induced potential acts as a two-level model that modifies the phonon scattering. The higher energy level represents the thermal excitation of the wrinkle. It is reasonable to assume that the higher energy level would be relieved or degenerated with decreasing distance between the wrinkle, as this would make the wrinkle easier to excite and create more resistance. The excited energy is stored inside the wrinkle through elastic deformation. This explains the singularity-like feature of this term in the equation. Furthermore, it provides a satisfactory picture of the temperature profile dependence in the effective heat conduction equation, as it leads to a possible non-reciprocal transport. The large thermal gradient characterized by the local effective temperature gradient leads to higher excitations via the $\partial T(x,t)/\partial x \cdot \partial k/\partial x$ term where $\partial k/\partial x$ can be understood as the gap between the two levels and

$\partial T(x,t)/\partial x$ represents the different excitations. The asymmetric position of the wrinkle introduces inversion-symmetry breaking which enables the non-reciprocal transport.

Wrinkles also significantly impact the TBC between the thin film and the substrate. While a comprehensive theoretical framework describing the influence of defects, including wrinkles, on TBC is lacking, we qualitatively outline the potential mechanisms behind these effects. Due to their characteristic size being in the micron scale, wrinkles induce residual strain fields extending over large areas such that strain effects typically propagate over long ranges in elastic media. These residual strain fields disrupt the uniformity of the interface affecting both the mechanical contact and the vibrational coherence between the thin film and the substrate. There are two main ideas behind this disruption. First, the wrinkle may reduce the effective contact area between the two materials which creates localized thermal resistances that collectively lower the overall TBC. Second, the residual strain may alter the atomic-scale interactions at the interface which weakens the phonon coupling and introduces additional scattering sites thereby hindering phonon transmission across the interface. Furthermore, the strain field spreading from the wrinkle may cause spatial variations in the elastic properties of the interface. These variations could exacerbate phonon mismatches and scattering and lead to a reduction in the efficiency of heat transfer. As a result, the presence of a wrinkle not only affects the immediate vicinity of the defect, but can also degrade the sensitive TBC across the entire detected region.

S11. Numerical simulation of the thermal model

As discussed in a previous section, we neglect the experiment data contained in the first ∼8 ns of the experiment and wait for after the thermal redistribution within the thin film along the cross-plane direction. We extract the corresponding temperature profile at different spatial positions after the initial redistribution period to construct the discretized initial temperature profile with the experimental noise. Afterwards, we fit and smooth the temperature profile with an exponential function $A \cdot e^{\frac{x-b}{\tau}}$ to simulate the thermal pump where A, b, τ are the fitting parameters. For the homogeneous transport without wrinkles, we assume $b = 0$. The temperature profile with the wrinkle is asymmetrical due to the presence of the wrinkle acting as a heat source or sink. To treat the initial temperature profile of this scenario, we separate the profile at the maximal point and fit the separated temperature profile correspondingly with the exponential function to reflect the asymmetrical feature.

We simulate the results by numerically solving the governing equations of the previous sections with the finite difference method. The wrinkle-induced thermal conductivity is simulated through a

triangle-like function with the spike sitting at the wrinkle position. To simplify the calculation, the thermal conductivity is considered homogeneous on each grid point except for those that correspond to positions around the wrinkle. We attempt to solve the equations with the forward Euler scheme of the finite difference method while simultaneously accounting for both the wrinkle and the special boundary condition caused by the TBC. We discretize using

$$\begin{aligned} \delta T_{2,\mathbf{s}}(\mathbf{r}, i) &= T(\mathbf{r} + \mathbf{s}, i) - T(\mathbf{r}, i) \\ \delta T_{1,\mathbf{s}}(\mathbf{r}, i) &= T(\mathbf{r}, i) - T(\mathbf{r} - \mathbf{s}, i) \end{aligned} \tag{S10}$$

where $T(\mathbf{r}, i)$ represents the local temperature profile at position $\mathbf{r}$, time i, and $\mathbf{s}$ represents the unit vector of the axis x, y, z. The external boundary condition is imposed through $T(\mathrm{b_{s,e}}, i) = 300$ K ($\mathrm{b_{s,e}}$ indicates the position at the boundary between the system and the external environment). The spatial derivatives are approximated as

$$\begin{aligned} \frac{\partial T(\mathbf{r}, i)}{\partial s} &\approx \frac{\delta T_{2,\mathbf{s}}(\mathbf{r}, i) + \delta T_{1,\mathbf{s}}(\mathbf{r}, i)}{2\delta s} \\ \frac{\partial^2 T(\mathbf{r}, i)}{\partial x^2} &\approx \frac{\delta T_{2,\mathbf{s}}(\mathbf{r}, i) - \delta T_{1,\mathbf{s}}(\mathbf{r}, i)}{(\delta s)^2} \end{aligned} \tag{S11}$$

where s represents the different components x, y, z. δs is the corresponding grid spacing. The time derivative is approximated as

$$\frac{\partial T(\mathbf{r}, i)}{\partial t} \approx \frac{T(\mathbf{r}, i+1) - T(\mathbf{r}, i)}{\delta t} \tag{S12}$$

where δt is the step size in the time domain. The forward Euler scheme is expressed as

$$\begin{aligned} T(\mathbf{r}, i+1) = T(\mathbf{r}, i) &+ \frac{\delta t}{C\rho} \sum_s \frac{k_{ss}(T(\mathbf{r} + \mathbf{s}, i) - 2T(\mathbf{r}, i) + T(\mathbf{r} - \mathbf{s}, i))}{(\delta s)^2} \\ &+ \frac{\delta t}{C\rho} \frac{k_{xx}(\mathbf{r} + \hat{\mathbf{x}}) - k_{xx}(\mathbf{r} - \hat{\mathbf{x}})}{2\delta x} \frac{T(\mathbf{r} + \hat{\mathbf{x}}, i) - T(\mathbf{r} - \hat{\mathbf{x}}, i)}{2\delta x}. \end{aligned} \tag{S13}$$

Notice that we only assume the wrinkle affecting the thermal conductivity along the x direction. $\hat{\mathbf{x}}$ is the unit vector along the x-axis. The mass density and the heat capacity of GaN are taken to be 6.08 g/cm^3 and 35.4 J/mol K at room temperature [3], respectively. The spatial mesh spacing $\delta x = \delta y = \delta z$ is taken to be 1 μm to correspond with the experimental setup and the temporal mesh spacing δt is 0.5 ns. We set this large spatial mesh spacing to simplify the simulation by ignoring the detailed temperature profiles reliant on the thin film thickness dependence. This is equivalent to assuming that the temperature distribution along the out-of-plane (z) direction of the thin film is uniform, which is reasonable after we reset the initial simulation time after several ns to allow the z-direction thermal redistribution to reach a uniform distribution. For the homogeneous region, the

stability of the forward Euler scheme requires $\delta t \leq ((\delta x)^2 C\rho)/(2k_{xx}+2k_{yy}+2k_{zz})$ from von Neumann stability analysis. Based on our numerical setup and assuming $k_{xx} = k_{yy} = k_{zz}$, the highest-tolerated thermal conductivity for the forward Euler scheme is calculated to be 856.67 W/m·K, much larger than our situation. We will take the calculated thermal conductivity bound of the forward Euler scheme as the approximate algorithmic stability bound.

We discuss how to implement the TBC calculation. We add two "virtual layers" between the two interface layers: one belongs to the GaN thin film and the other one belongs to the Si substrates. From top to bottom, we have the first computing layer representing the thin film GaN which grows on the substrate. Following this layer is a virtual one added for calculating the heat flux from the GaN thin film to the substrate, followed by another virtual layer for the Si substrate. Lastly, there is the top layer of the Si substrate representing the real temperature profile at that location. The temperature difference at the boundary should be the corresponding one between the top layer representing GaN thin film and the overall fourth layer,r representing the top layer of the Si substrate. The two virtual layers are only present for calculating the directional temperature gradient conveniently and are not reflective of real temperature profiles. To discretize the boundary condition, we have

$$\begin{aligned} -k_{zz,\mathrm{GaN}}\frac{T_{\mathrm{GaN,b}}(i+1)-T_{\mathrm{GaN,v}}(i+1)}{\delta z} &= G_{\mathrm{GaN,Si}}(T_{\mathrm{Si,b}}(i+1)-T_{\mathrm{GaN,b}}(i+1)), \\ -k_{zz,\mathrm{Si}}\frac{T_{\mathrm{Si,b}}(i+1)-T_{\mathrm{Si,v}}(i+1)}{\delta z} &= G_{\mathrm{GaN,Si}}(T_{\mathrm{GaN,b}}(i+1)-T_{\mathrm{Si,b}}(i+1)) \end{aligned} \tag{S14}$$

where $T_{\mathrm{Si,b}}$ and $T_{\mathrm{GaN,b}}$ are calculated from the numerical scheme of the heat conduction equation mentioned above, $T_{\mathrm{Si,v}}$ and $T_{\mathrm{GaN,v}}$ are the temperature profiles at the virtual layer. Note that when calculating the Laplacian of the actual boundary layer, we take the temperature profile of the virtual layer at the time step i to help determine the Laplacian through the gradient. As a result, we only need to calculate the temperature profile for the virtual layer from the boundary condition, which is equivalent to solving a linear system above. This determines the temperature on the virtual layer and fixes the heat flux to keep this boundary condition at each time step. This virtual layer can also apply to the boundary between the system and the external environment by assuming thermal insulation. This is equivalent to having the corresponding TBC equal to 0 and fixing the environment temperature as $T_{\mathrm{env}} = 300$ K.

To determine the thermal conductivity from the experimental data, we design the evaluation loss function to characterize the deviation between the simulated spatial and time-resolved temperature profiles and the experimental data. By solving the optimization problem of this loss function, we determine the best-fitted thermal conductivity parameters. We use the residue as well as the first spatial and time derivatives of the temperature profile between the theoretically calculated results

and the experimental data. We also add the correction term to reduce the deviation between the experimental data and the simulation of the largest temperature difference within the temperature profile at a fixed time, which represents how quickly the overall heat dissipates in the system. Here, we choose the pump-probe direction along the x-axis to simplify the comparison between experimental data and the modeling temperature profile. The comparison then reduces to the case of one spatial dimension along x_i and one temporal dimension along t_j. The loss function can be written as

$$\begin{aligned}\mathcal{L} =& \sum_{x_i,t_j} |T_{\mathrm{m}}(x_i,t_j) - T_{\mathrm{s}}(x_i,t_j)| + \sum_{x_i,t_j} \left| \frac{\partial T_{\mathrm{m}}(x_i,t_j)}{\partial x_i} - \frac{\partial T_{\mathrm{s}}(x_i,t_j)}{\partial x_i} \right| + \sum_{x_i,t_j} \left| \frac{\partial T_{\mathrm{m}}(x_i,t_j)}{\partial t_j} - \frac{\partial T_{\mathrm{s}}(x_i,t_j)}{\partial t_j} \right| \\ &+ \sum_{t_j} \left| \left(\max_{x_i} T_{\mathrm{m}}(x_i,t_j) - \min_{x_i} T_{\mathrm{m}}(x_i,t_j) \right) - \left(\max_{x_i} T_{\mathrm{s}}(x_i,t_j) - \min_{x_i} T_{\mathrm{s}}(x_i,t_j) \right) \right|\end{aligned} \tag{S15}$$

where T_{m} and T_{s} are the experimentally measured and calculated temperature profiles, respectively.

To determine the in-plane thermal conductivity of the GaN film, we first fix the TBC and cross-plane thermal conductivity of the film extracted from the TDTR experiments as $k_{\perp} = 65$ W/m·K and 2.82×10^7 W/m^2·K. We use the experimental data without the wrinkle and calculate the loss function over the whole range to find the minimized value. The minimization algorithm can be a gradient-based method such as the limited-memory Broyden–Fletcher–Goldfarb–Shanno algorithm, which can be used directly from the Python-based scipy.optimize package.

However, this loss function does not apply appropriately for the wrinkle case as it will lead to highly suppressed in-plane thermal conductivity or TBC which is inconsistent between the experimental temperature profile and the simulated one. To correct this, we impose another condition which is to take the curvature of the temperature profile around the wrinkle position into account. This means we add the correction factor for the curvature around the wrinkle site defined as

$$\mathcal{L}_{\mathrm{c}} = \left| \frac{\partial^2 T_{\mathrm{m}}}{\partial x^2} - \frac{\partial^2 T_{\mathrm{s}}}{\partial x^2} \right|. \tag{S16}$$

Only considering the experiments related to the wrinkle will cause overfitting: the fitted results will diminish TBC or the in-plane conductivity around the wrinkle part individually. This fit does not reflect the features observed from the experimental data, which are notably, the asymmetric transport caused by the change of the in-plane thermal conductivity locally around the wrinkle and the total reduction of the thermal dissipation. To address this issue of overfitting, we add regularization to the loss function and assume the change of the TBC is relatively small due to the possible residual strain field. We add the loss function for the experimental data without wrinkle to fit TBC and the in-plane conductivity around the wrinkle simultaneously. The loss function becomes

$$\mathcal{L}_{\mathrm{tot}}(G_{\mathrm{GaN,Si}}, k_w) = \mathcal{L}_{\mathrm{non-wrinkle}}(G_{\mathrm{GaN,Si}}, k_w) + \mathcal{L}_{\mathrm{wrinkle}}(G_{\mathrm{GaN,Si}}, k_w). \tag{S17}$$

We require the change of the TBC due to the wrinkle to be relatively small to avoid overfitting and the TBC is regularized by the case without a wrinkle. To characterize the contribution of the wrinkle, we fix the thermal conductivity determined from the experiment without the wrinkle and allow the local change of the thermal conductivity and the TBC. We determine the sets of values that minimizes the loss function after scanning through the entire parameter space for these parameters. This loss function may have a very complex landscape such that the gradient-based optimization algorithm may not be proper for this situation. In that case, a differential evolution method, which is a meta-heuristic global optimization algorithm, may find superior usage. To ensure that the algorithm converges to the global minimum, we run the algorithm ten times to determine the final parameters. The error bar for these parameters is obtained by fixing the other two parameters through the error bound obtained from experimental data.

To validate the necessity of fitting both the TBC and the local thermal conductivity around the wrinkle simultaneously, we performed optimizations by varying each parameter individually. When fitting both parameters simultaneously, the optimization from wrinkle-related data yields residual errors of 65.05 and 25.27, respectively. In contrast, fitting only the local thermal conductivity around the wrinkle using the same data results in a fitted value of $k_w = 9.00$ W/m·K with higher corresponding residual errors of 66.02 and 26.39. For the case of fitting only the TBC, the optimized TBC value is 9.45×10^6 W/m^2·K with an even higher residual error of 70.52. These results demonstrate that simultaneous fitting of both TBC and k_w provides an improved match to the experimental data, all while underscoring the importance of considering the impact of the wrinkle on the TBC. For the case of the corrected conversion of the data to the local temperature, the residual errors are 45.20 and 17.56 for the simultaneous fit, while it's 45.88 and 18.32 for the single fit of the local thermal conductivity around the wrinkle. For the case of ftting only the TBC, the optimized TBC value is 9.48×10^6 W/m^2·K with an even higher residual error of 48.98. These results align well with the original case, while the residual errors are reduced perhaps due to the improved temperature calibration but not affect the final fitted results a lot.

S12. Monte Carlo fitting algorithm results of FDTR measurements

The error on the thermal conductivity and the TBC from FDTR quoted in the main text is representative of a confidence interval from performing the Monte Carlo fit 1000 times and obtaining the width of the spread in Fig. S11. As the experimental measurement is repeated on different spots on the sample, the standard deviation of the fitted spread value from different spots provides the true

experimental error bar. In the text, we use the confidence interval as an upper bound to emphasize the error of the FDTR technique at a single spot.

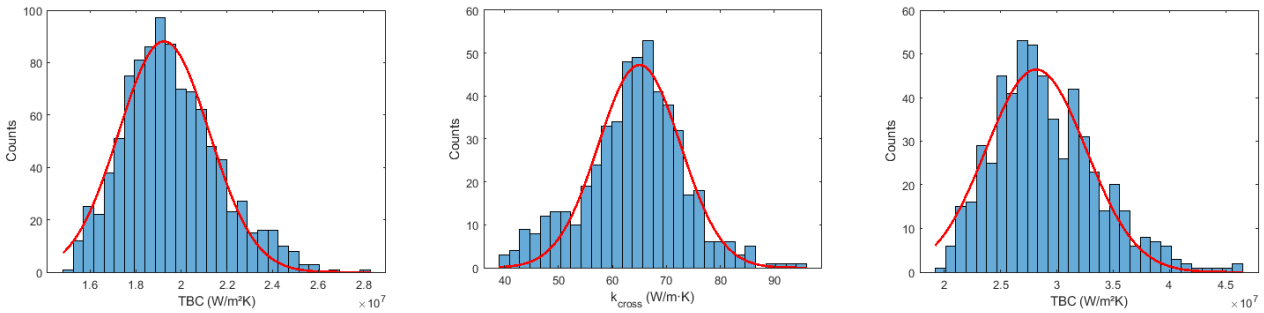

Figure S11. Plots of the Monte Carlo fitting algorithm with histogram counts representing the fitted values and error spread for the Au/GaN thermal boundary conductance (left), the cross-plane thermal conductivity of GaN (middle) fitted as $k_{||} = (92.8 \pm 22.0)$ W/m·K, and the GaN/Si thermal boundary conductance (right) fitted as $G = (2.8 \pm 0.2) \times 10^7$ W/m^2·K.

S13. Literature on thermal conductivity of gallium nitride

In this supplementary note, we provide a table of previous literature values of thermal conductivity of GaN in both bulk and thin film forms and on different substrates to serve as a comparison to our study. We note that the table is not comprehensive with the entire literature on GaN thermal transport. These values are plotted in Fig. 4c of the main text.

Table S1. Compilation of values (or ranges of values) of the thermal conductivity and thermal boundary conductance of GaN at room temperature on different substrates and thicknesses found in a subset of literature.

Substrate	**Thickness (nm)**	k **(W/m·K)**	**Reference**
Si	500	92.8 ± 22.0	This work
Bulk	Bulk	240 ± 20	[4–7]
Si	1200	150 ± 22.5	[8]
GaN	250-2100	150-195	[9]
GaN/sapphire	400-800	55-167	[9]
AlN/sapphire	3190	162 ± 16	[10]
Sapphire	3520	190 ± 15	[10]
4H-SiC	14-940	2-118	[11]
AlN/SiC	900	167 ± 15	[12]
AlN/Si	1300	185 ± 20	[12]

[1] G. Chen, *Nanoscale energy transport and conversion: a parallel treatment of electrons, molecules, phonons, and photons* (Oxford University Press, Oxford, 2005).

[2] E. Weinan, *Principles of multiscale modeling* (Cambridge University Press, Cambridge, 2011).

[3] N. M. Ravindra, S. R. Marthi, and A. Bañobre, *Radiative Properties of Semiconductors* (Morgan & Claypool Publishers, 2017).

[4] A. Jeżowski, B. A. Danilchenko, M. Boćkowski, I. Grzegory, S. Krukowski, T. Suski, and T. Paszkiewicz, *Thermal conductivity of GaN crystals in 4.2–300 K range,* Solid State Commun. **128**, 69 (2003).

[5] C. Mion, J. F. Muth, E. A. Preble, and D. Hanser, *Accurate dependence of gallium nitride thermal conductivity on dislocation density,* Appl. Phys. Lett. **89**, 092123 (2006).

[6] R. B. Simon, J. Anaya, and M. Kuball, *Thermal conductivity of bulk GaN—Effects of oxygen, magnesium doping, and strain field compensation,* Appl. Phys. Lett. **105**, 202105 (2014).

[7] A. Jeżowski, O. Churiukova, J. Mucha, T. Suski, I. A. Obukhov, and B. A. Danilchenko, *Thermal conductivity of heavily doped bulk crystals GaN:O. Free carriers contribution,* Mater. Res. Express **2**, 085902 (2015).

[8] A. Sarua, H. Ji, K. P. Hilton, D. J. Wallis, M. J. Uren, T. Martin, and M. Kuball, *Thermal Boundary Resistance Between GaN and Substrate in AlGaN/GaN Electronic Devices,* IEEE Trans. Electron De-

vices **54**, 3152 (2007).

[9] Y. R. Koh, M. S. B. Hoque, H. Ahmad, D. H. Olson, Z. Liu, J. Shi, Y. Wang, K. Huynh, E. R. Hoglund, K. Aryana, J. M. Howe, M. S. Goorsky, S. Graham, T. Luo, J. K. Hite, W. A. Doolittle, and P. E. Hopkins, *High thermal conductivity and thermal boundary conductance of homoepitaxially grown gallium nitride (GaN) thin films,* Phys. Rev. Mater. **5**, 104604 (2021).

[10] H. Li, R. Hanus, C. A. Polanco, A. Zeidler, G. Koblmüller, Y. K. Koh, and L. Lindsay, *GaN thermal transport limited by the interplay of dislocations and size effects,* Phys. Rev. B **102**, 014313 (2020).

[11] E. Ziade, J. Yang, G. Brummer, D. Nothern, T. Moustakas, and A. J. Schmidt, *Thickness dependent thermal conductivity of gallium nitride,* Appl. Phys. Lett. **110**, 031903 (2017).

[12] J. Cho, Y. Li, W. E. Hoke, D. H. Altman, M. Asheghi, and K. E. Goodson, *Phonon scattering in strained transition layers for GaN heteroepitaxy,* Phys. Rev. B **89**, 115301 (2014).